Title

Investigation of Hierarchical Structure Formation in Merocyanine Photovoltaics

Journal

The Journal of Physical Chemistry C, 124(36)

ISSN

1932-7447

Authors

Murrey, Tucker L

Hertel, Dirk

Nowak, Julian

et al.

Publication Date

2020-09-10

DOI

10.1021/acs.jpcc.0c04988

Peer reviewed

THE JOURNAL OF PHYSICAL CHEMISTRY C

pubs.acs.org/JPCC Article

Investigation of Hierarchical Structure Formation in Merocyanine Photovoltaics

Tucker L. Murrey, Dirk Hertel, Julian Nowak, Ruth Bruker, Thorsten Limböck, Jörg Neudörfl, Stephanie Rüth, Jürgen Schelter, Selina Olthof, Aurel Radulescu, Adam J. Moulé,* and Klaus Meerholz*

Cite This: https://dx.doi.org/10.1021/acs.jpcc.0c04988 Read Online

ACCESS | Metrics & More | Article Recommendations | Supporting Information

ABSTRACT: Merocyanines (MCs) are a versatile class of small-molecule dyes. Their optoelectronic properties are easily tunable by chemically controlling their donor−acceptor strength, and their structural properties can be tuned by simple side-chain substitution. This manuscript demonstrates a novel series of MCs featuring an indoline donor with varying hydrocarbon side-chain length (from 6 to 12 carbons) and a *tert*-butyl-thiazole acceptor, labeled I*n*TBT. Bulk heterojunction organic photovoltaics are fabricated with a [6,6]-phenyl-C_{61}-butyric acid methyl ester (PCBM) acceptor and characterized. Films composed of I8TBT:PCBM and I9TBT:PCBM produced the highest power conversion efficiency of 4.5%, which suggests that the morphology is optimized by controlling the side-chain length. Hierarchical structure formation in I*n*TBT:PCBM films is studied using grazing incidence X-ray diffraction (GIXRD), small-angle neutron scattering (SANS), and atomic force microscopy (AFM). When mixed with PCBM, I*n*TBTs with ≤8 side-chain carbons form pure crystalline domains, while I*n*TBTs with ≥9 side-chain carbons mix well with PCBM. SANS demonstrates that increasing side-chain length increases the I*n*TBT-rich domain size. In addition, a branched hexyl−dodecyl side-chain IHDTBT:PCBM film was studied and found to exhibit the worst-performance organic photovoltaic (OPV) device. The large-branched side chain inhibited mixing between IHDTBT and PCBM resulting in large segregated phases.

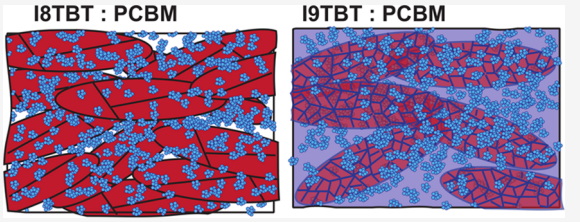

INTRODUCTION

An increasing number of donor candidate molecules for organic photovoltaics (OPVs) with alternating electron donor (D) and acceptor (A) subunits have been reported in recent years.[1−4] Among simple dyes, dipolar merocyanines (MCs) are an interesting and versatile class of functional materials.[5,6] MC donor−acceptor (D−A) groups can be easily changed to tune their absorption from the blue to IR spectral region, with ground-state dipole moments ranging from 3 to 15 D. MCs have been applied as active component in bulk heterojunction (BHJ) OPV devices.[7−10] A previous study by Kronenberg et al. showed that BHJ OPVs composed of indoline-based MC donors and [6,6]-phenyl-C_{61}-butyric acid methyl ester (PCBM) or C_{60} acceptors manifest in large open-circuit voltages (V_{OC}) and short-circuit currents (J_{SC}) of 0.9, 0.76 V and 5.3, 6.3 mA/cm^2, respectively. However, poor charge transport gave rise to low fill factors (FFs) (∼30%) resulting in power conversion efficiencies (PCEs) of 1.5 and 1.7%.[11] Subsequently, Steinmann et al. created a tandem OPV using the same materials resulting in a very high V_{OC} of 2.1 V and a PCE of 4.8%, but retained a low FF.[12] So far, the highest PCE reported from an indoline-based D−A device with a simple BHJ architecture is 6.1% (FF 47%) from a vacuum-deposited MC:PCBM device, while the record for a solution-processed device is 4.5%.[13,14] Both of these devices benefited from improved FFs of 47 and 44%, respectively.

Morphology control is currently a major limitation for D−A OPVs. A variety of structural motifs have been obtained for several D−A subunits with varying dipole strengths, including but not limited to simple isolated antiparallel dimers, stacked dimers (1D), and slipped/staircase-like structures.[14,15] Due to the complexity of interactions between neighboring molecules (i.e., competing sterical interactions, intermolecular van der Waals/dipolar forces, and substrate interactions), there is currently no set of guidelines capable of predicting the solid-state packing from molecular structure. Recently, many new small-molecule architectures have been developed to prevent D−A dipole alignment and improve $\pi-\pi$ stacking including donor−acceptor−donor (D−A−D) and acceptor−donor−acceptor (A−D−A).[16] The current BHJ OPV record for a small-molecule device is held by an A−D−A donor molecule with π-conjugated bridges between the groups denoted as A−π−D−π−A, with a PCE of 14.3%.[17] The cost of synthesizing A−π−D−π−A molecules is considerably larger

Received: June 2, 2020
Revised: July 22, 2020
Published: July 29, 2020

than for simple D−A compounds. Research to improving the BHJ morphology with simple D−A donors is necessary.

Optimizing the structural properties of D−A BHJ OPVs is challenging. To enable efficient charge separation and collection, p-type MC donors must be mixed with an n-type acceptor (i.e., PCBM). The mixture of MC:PCBM in the solid state can create a multiphase system with pure MC, pure PCBM, and mixed domains. Domain size, crystal structure, and domain purity must be optimized to promote efficient exciton dissociation, charge transport, and extraction.[18]

In this article, we report a comprehensive investigation of a series of structurally related D−A MC dyes, with varying hydrocarbon side-chain length (Figure 1). The choice of MC is

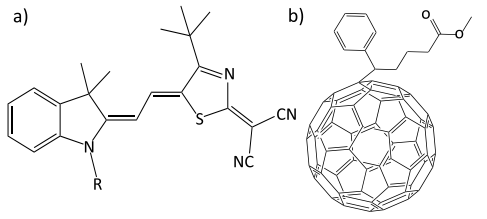

Figure 1. Chemical structures of compounds used in this study: (a) a series of MC featuring an indoline donor with varying hydrocarbon side-chain length (R) and a *tert*-butyl-thiazole acceptor, labeled I*n*TBT. (b) $PC_{61}BM$.

based on previous studies, which obtained best results, in terms of PV performance, with indoline-based donor groups.[2,3] The thiazol-di-cyanovinylene acceptor group was chosen because its high acceptor strength enables H/J-type coupling,[19] shows high mobility in crystalline OFETs, and yields a high V_{OC} with PCBM due to favorable ionization energy.[3] By tuning the side-chain length, we are able to control solubility, molecular packing, and phase segregation in MC:PCBM BHJ OPV devices. The BHJ films are characterized in OPV devices to obtain $J-V$ curves, and structural information is obtained using grazing incidence X-ray diffraction (GIXRD), small-angle neutron scattering (SANS), and atomic force microscopy (AFM). Similar to previous studies,[20−22] we show that by tuning the hydrocarbon side-chain length we can control the hierarchical structure formation to improve charge extraction in MC-based OPVs.

METHODS

Sample Processing. All OPVs were fabricated on indium-tin oxide (ITO, 125 nm)-coated glass. The substrates were exposed to ozone for 3 min and transferred to the evaporation chamber to evaporate 10 nm MoO_3. Substrates were transferred into a glovebox to spin-coat 70 nm thick active layers from chloroform solutions of 13−15 mg/mL mixed in a ratio of 2:3 (I*n*TBT to $PC_{61}BM$). The device fabrication was completed by thermal evaporation of 5 nm Ca and then 100 nm Ag.

UV−Vis. Absorption measurements were performed using a Lambda 1050 (Perkin Elmer) UV/vis spectrometer. A molar concentration of 10^{-4}−10^{-6} mol/L was used for performing optical absorption measurements in solution.

Single-Crystal XRD. Measurement of single crystals was done using a Bruker D8 Venture (with software APEX3) in kappa geometry equipped with a copper microfocus source and a Photon100 detector. SADABS[23] was used for analysis, scaling, and absorption correction. SHELXT and SHELXL[24] were used for I*n*TBT structure refinement.

GIXRD. GIXRD was collected using a Panalytical Empyrean system with a Cu Kα anode λ = 1.54056 Å. Glass was used as the amorphous substrate. The incidence angle was optimized for every measurement to reduce scattering from the substrate and air interfaces. Initially, a survey was conducted from $2\theta \sim$ 5 to 15° with ω = 0.2°. The most intense 2θ peak was used to find the optimal ω for signal and background measurement.[25]

SANS. The SANS experiments were completed on a KWS-2 SANS instrument at the Heinz Maier-Leibnitz Zentrum (MLZ), Garching, Germany. Three instrument conditions were used to provide Q-values ranging from 0.16 to 0.003 Å^{-1}, where $Q = \frac{4\pi}{\lambda}\sin\left(\frac{\theta}{2}\right)$; λ is the neutron wavelength and θ is the scattering angle. The first two conditions were collected with a collimation length of 4 m with a neutron wavelength of 4.66 Å and sample−detector distances of 1.61 and 3.61 m. For the third condition, the collimation length was 20 m with neutron wavelength 5 Å and the sample−detector distance at 19.51 m.

AFM. The AFM measurements were performed on an MFP-3d Infinity from Asylum Research. All measurements were conducted in an amplitude-modulated alternating contact mode utilizing microcantilevers of the type OMCL-AC200TS from Olympus Micro Cantilevers. All measurements were conducted under ambient conditions in air.

RESULTS

The procedures to synthesize the MC donors can be found in the Supporting Information. We synthesized a series of MCs with varied side-chain length on the indolene from hexyl to dodecyl and a derivative with a branched hexyl−dodecyl chain. For the ease of labeling, we number the MCs according to the side-chain length, i.e., I*n*TBT, with I6TBT for the hexyl side chain and so on to I12TBT and IHDTBT for the branched derivative (see Figure 1). The I*n*TBTs with $n > 6$ have a much higher FF (FF > 0.6) compared to typical MC cells processed from solution/or vacuum of comparable thickness (Figure 3a).[26]

The side chain affects both the solubility and crystal packing but does not change the optical or electronic properties of the dye itself. All I*n*TBT samples have nearly identical UV−vis absorbance at the same molar concentration and solvent quality in solution. The absorption spectra of I8TBT in solutions with varying polarity are shown in Figure S5. The data shows a clear progression from a blue-shifted spectrum in hexane to red-shifted J-aggregates in more polar solvents. Since the I*n*TBTs are less soluble in nonpolar solvents, this progression also shows that a red-shifted UV−vis spectrum with an increased 0−0 to 0−1 peak ratio indicates the presence of ordered crystalline aggregates in the film.[10,19] Figure 2 shows UV−vis absorption spectra of all 40:60 wt% I*n*TBT:PCBM films normalized to the central peak at 590 nm. In these aggregates, the coupling between nearest neighbors is strongly influenced by the side-chain length.

A clear side-chain length trend can be observed in the UV−vis data. The OPV films all share three MC vibronic peaks at ∼650 nm (0−0), ∼600 nm (0−1), and ∼550 nm (0−2), as well as a PCBM peak at ∼350 nm. The linear side-chain samples also share an amorphous absorption at ∼500 nm. The spectra are normalized to the central peak of the MC, which allows us to probe the symmetry of the D−A aggregations to be more H-like or J-like and provides information on

https://dx.doi.org/10.1021/acs.jpcc.0c04988
J. Phys. Chem. C XXXX, XXX, XXX−XXX

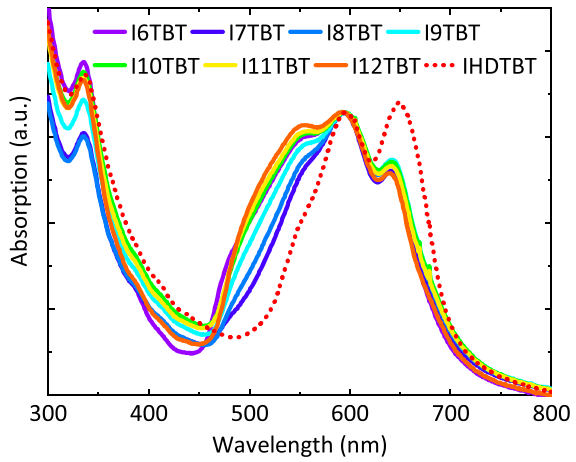

Figure 2. UV−vis absorption spectra of I*n*TBT:PCBM films normalized to the common peak at 594 nm.

delocalization. The ratio of the 0−0 to 0−1 transitions $\left(\frac{0-0}{0-1}\right)$ is fairly constant for all of the I*n*TBTs with linear side chains, meaning the aggregations are similar in orientation. As the linear side chain increases in length, the 0−2 peak and amorphous absorption increase, indicating that the I*n*TBTs with longer side chains experience additional geometries. The 0−0 and 0−1 transition ratios in the IHDTBT:PCBM film depict a J-like configuration indicating minimal mixing with PCBM.

We fabricated BHJ OPV devices from solution with I*n*TBT:PCBM in a composition ratio of 2:3 by weight, which means the molar ratio changes as a function of side-chain length.[27] The active layer thickness was kept at a constant 70 nm for all of the devices due to the limited solubility of the short and very long side-chain derivatives. The hole collection layer is 10 nm MoO_3 evaporated onto ITO,[3] and the anode is composed of 5 nm Ca/100 nm Ag. All of the device fabrication details are in the experimental section. Typical AM1.5 solar simulator *JV* curves are shown in Figure 3a for all I*n*TBT:PCBM devices. The *JV* characteristics are listed in Table 1, and PCE as a function of side-chain length is shown in Figure 3b.

As the I*n*TBT side-chain length is increased from 6 to 12 carbons, the V_{OC} increases to a maximum at 0.90 ± 0.01 V for I9TBT, I10TBT, and I11TBT before decreasing again. The I6TBT device has the highest short-circuit current density (J_{sc}) at 8.29 ± 0.38 mA/cm^2 because it has the highest absorbance integral (shortest side chain) seen in the unnormalized UV−vis (Figure S6). I11TBT has the highest FF at 0.67 ± 0.01, indicating the most favorable balance of hole and electron transport.[28,29] The highest PCE of 4.5 ± 0.1% was extracted from devices with I8TBT and I9TBT. These films exhibited the best combination of J_{sc} and FF, balancing increased optical absorbance for short side chains and favorable morphology for longer chains. Higher PCE devices could be obtained by optimizing layer thickness and the mixing ratio for I8TBT-I12TBT; however, this is not the goal of this study. Rather, we focus on explaining how the side-chain length affects the morphology in this material class. The MC with the branched side-chain IHDTBT exhibited the worst device performance in spite of the most favorable absorbance.

To probe the smallest length scale structures (Å) in pure I*n*TBT and 2:3 I*n*TBT:PCBM films, we use grazing incidence

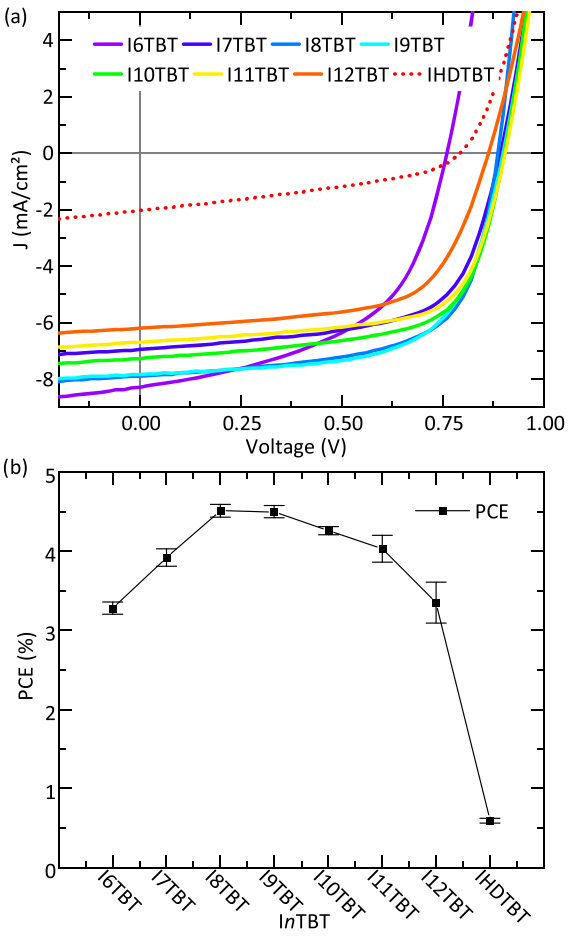

Figure 3. (a) *JV* curves and (b) extracted power conversion efficiencies by wt ratio of 2:3 I*n*TBT:PCBM devices.

Table 1. Best Performance Data of I*n*TBT:PCBM OPVs in the Standard Device Setup (Composition 2:3)

Merocyanine	V_{OC} (V)	J_{sc} (mA/cm^2)	FF	PCE (%)
I6TBT	0.76 ± 0.01	8.29 ± 0.38	0.52 ± 0.02	3.3 ± 0.1
I7TBT	0.89 ± 0.01	6.95 ± 0.15	0.63 ± 0.01	3.9 ± 0.1
I8TBT	0.89 ± 0.01	7.90 ± 0.24	0.64 ± 0.02	4.5 ± 0.1
I9TBT	0.90 ± 0.01	7.83 ± 0.22	0.64 ± 0.02	4.5 ± 0.1
I10TBT	0.90 ± 0.01	7.28 ± 0.13	0.65 ± 0.01	4.3 ± 0.1
I11TBT	0.90 ± 0.01	6.69 ± 0.28	0.67 ± 0.01	4.0 ± 0.1
I12TBT	0.86 ± 0.01	6.20 ± 0.3	0.63 ± 0.02	3.4 ± 0.3
IHDTBT	0.79 ± 0.01	2.03 ± 0.06	0.37 ± 0.02	0.6 ± 0.1

X-ray diffraction (GIXRD) (Figures S7−S23). Diffraction peaks were fit with a pseudo-Voigt model to extract peak positions and widths.[30,31] Bragg's law was used to calculate the crystal *d*-spacing, and the Scherrer equation was used to calculate coherence length (L_C) for the most prominent I*n*TBT and PCBM peaks (Tables 2 and S19).[32−34] GIXRD of the pure PCBM film shows two peaks at $2\theta \sim 19.5$ and $\sim 9.7°$, in accordance with the literature.[35]

In the pure I*n*TBT films, the samples with side chains $n \leq 8$ form larger crystals with L_C >14 nm (Table 2). In I*n*TBT samples with side chain $n \geq 9$ (and IHDTBT), the side chain is long enough to impede crystal growth, thereby reducing the L_C <8.2 nm. In the I*n*TBT:PCBM films, the I*n*TBT L_C decreases significantly in all of the studied samples, suggesting that I*n*TBTs form smaller more disordered crystals when

https://dx.doi.org/10.1021/acs.jpcc.0c04988
J. Phys. Chem. C XXXX, XXX, XXX−XXX

Table 2. Bragg's d-spacing and Scherrer's Coherence Length L_C Extracted from the Most Prominent I*n*TBT Peak (in the Range of $2\theta \sim 4-10°$) from Pure and Mixed I*n*TBT:PCBM Films

I*n*TBT	I*n*TBT *d*-spacing (Å)	I*n*TBT L_C (Å)	I*n*TBT:PCBM *d*-spacing (Å)	I*n*TBT:PCBM L_C (Å)
I6TBT	12.0 ± 0.1	147 ± 2	11.5 ± 0.1	41 ± 1
I7TBT	11.1 ± 0.1	220 ± 6	12.5 ± 0.1	75 ± 8
I8TBT	12.6 ± 0.1	181 ± 8	12.8 ± 0.1	87 ± 6
I9TBT	9.7 ± 0.1	56 ± 37	11.6 ± 0.1	11 ± 8
I10TBT	10.2 ± 0.1	39 ± 8	11.1 ± 0.1	17 ± 15
I11TBT	17.5 ± 0.1	82 ± 4	17.8 ± 0.1	42 ± 4
I12TBT	17.9 ± 0.1	40 ± 6	20.7 ± 0.1	39 ± 25
IHDTBT	20.8 ± 0.1	82 ± 3	21.1 ± 0.1	48 ± 27

mixed with PCBM (Table 2). The L_C of the PCBM peak at $2\theta \sim 19.5°$ remains consistent (~1.6 nm) in all of the I*n*TBT:PCBM films (Table S19), which shows that pure PCBM crystalline domains form in all films. The ratio of the prominent I*n*TBT to PCBM peak intensity in the mixed films is shown in Figure 4. I*n*TBTs with $n \leq 8$ and n = HD form

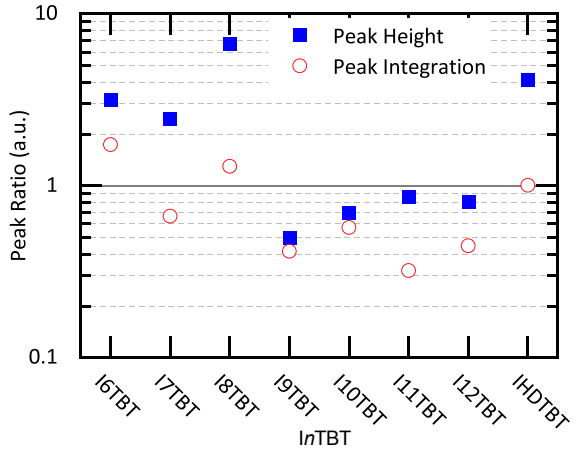

Figure 4. GIXRD: ratio of the prominent I*n*TBT peak over prominent PCBM peak (peak heights and peak integrations) in mixed 2:3 by wt ratio of I*n*TBT:PCBM films.

pure I*n*TBT crystalline domains in the presence of PCBM. Their prominent diffraction peak intensity around ~7.5° is 2–6 times greater than their corresponding PCBM peak intensity. As the linear side chain is increased to $n \geq 9$, the I*n*TBT peaks broaden significantly and the prominent peak height ratio $\left(\frac{\text{InTBT peak height}}{\text{PCBM peak height}}\right)$ decreases below unity (Figures 4 and S14–S21). A similar drop in the prominent peak integration ratio $\left(\frac{\text{InTBT peak integration}}{\text{PCBM peak integration}}\right)$ is observed, although the change is less discernible due to the broadening of the InTBT diffraction peaks and the large full width at half-maximum (FWHM) of the PCBM peak. This suggests that I*n*TBTs with linear side chains $n \geq 9$ undergo significant mixing with PCBM and form amorphous structures that do not have long-range order.

I*n*TBT diffraction peaks for $n \leq 8$ broaden and shift when mixed with PCBM, resulting in minor shifts in the prominent I*n*TBT *d*-spacing (Table 2). I6TBT *d*-spacing decreases from 12.0 Å to 11.5 Å, while both I7TBT and I8TBT *d*-spacings increase from 11.1 Å and 12.6 Å to 12.5 Å and 12.8 Å, respectively. More significant changes upon mixing are observed for I*n*TBTs with $n \geq 9$. The I9TBT peaks at 2θ = 4.64°, 5.31°, 7.06°, and 9.11° merge into a single broad peak at 7.63° when mixed with PCBM, resulting in the apparent I*n*TBT:PCBM *d*-spacing of 11.6 Å. The I10TBT peaks at 7.16° and 8.66° merge into the broad peak at 7.95° when mixed with PCBM, resulting in the apparent I*n*TBT:PCBM *d*-spacing of 11.1 Å. Upon mixing with PCBM, I11TBT peaks broaden and merge but are still distinguishable; the peaks at 4.25° and 5.05° shift to 4.02° and 4.95°, increasing the *d*-spacing to 22 Å and 17.8 Å, respectively. The peaks at 7.19° and 8.49° shift to 7.27° and 8.24°, changing the *d*-spacing to 12.2 Å and 10.7 Å, respectively. The I12TBT peaks at 4.04° and 4.93° merge into the broad peak at 4.26° when mixed with PCBM, resulting in the apparent I12TBT:PCBM *d*-spacing of 20.7 Å. Finally, upon mixing with PCBM, the IHDTBT peak shifts from 4.25° to 4.18° resulting in a *d*-spacing 21.2 Å. In summary, when mixed with PCBM, the I*n*TBTs with $n \leq 8$ remain phase-segregated and show minor broadening and shifting of their prominent diffraction peaks, while I*n*TBTs with $n \geq 9$ allow intercalation of PCBM into the I*n*TBT crystals causing a significant broadening of their diffraction peaks due to reduced long-range order.

We use SANS to probe the size, shape, and composition of nanoscale (3–200 nm) domains in I*n*TBT:PCBM films ($7 \leq n \leq 11$).[36] Differences in the ^{1}H density between I*n*TBT and PCBM lead to a neutron scattering contrast. Figure 5a shows SANS data ($I(Q)$ vs Q), where I is the intensity and Q is the momentum transfer in units of Å^{-1}. This scattering data is fit to a model that determines statistical length scale correlations and relative density differences between domains. SANS is not sensitive to crystallinity, which allows us to probe structural and compositional density distributions of the full bulk sample, not just the crystalline regions as for X-ray diffraction analysis.

The I*n*TBTs with linear side chains form elongated domains that are best fit with an ellipsoidal form factor.[37] We therefore use a model that assumes elongated InTBT-rich domains surrounded by the PCBM-rich material. Figure 5b depicts the parameters extracted from the fit, where R_S is the mean radius along the short axis of the ellipsoid, R_L is the mean radius along the long axis of the ellipsoid, and the scattering length density (SLD) contrast is a parameter describing the compositional difference between the ellipsoids and surrounding matrix. The log–normal domain size dispersity (SD) of R_S and R_L is displayed in Figures S24 and S25.

From the previously discussed GIXRD, I7TBT, and I8TBT, MCs form pure crystalline phases when mixed with PCBM. Since the SLD for neutrons depends on the atomic density and composition of each phase, the ellipsoid SLDs (Table S20) are estimated from unit cell information obtained from single-crystal simulations (Table S2). The SLD of a pure crystalline PCBM domain is also shown in Table S20.[38] The expected SLD contrast for pure I*n*TBT and PCBM domains is 3.3–3.4 × 10^{-6} Å^{-2}. Since the measured SLD contrast between the ellipsoidal I*n*TBT domains and the surrounding matrix is much smaller than expected for pure domains (~1.2 × 10^{-6} Å^{-2}) and since PCBM forms pure clusters that are too small to be detected with SANS (Table S19), the matrix is assumed to be a mixed I*n*TBT:PCBM domain. For I7TBT and I8TBT, the total volume fraction of the ellipsoidal domains ($\phi_{\text{Ellipsoid}}$) is determined with Equations S3 and S7 (Table 3), where the partial volume fractions of PCBM and I*n*TBT are known from solution concentrations. As the linear I*n*TBT side chain is

https://dx.doi.org/10.1021/acs.jpcc.0c04988
J. Phys. Chem. C XXXX, XXX, XXX–XXX

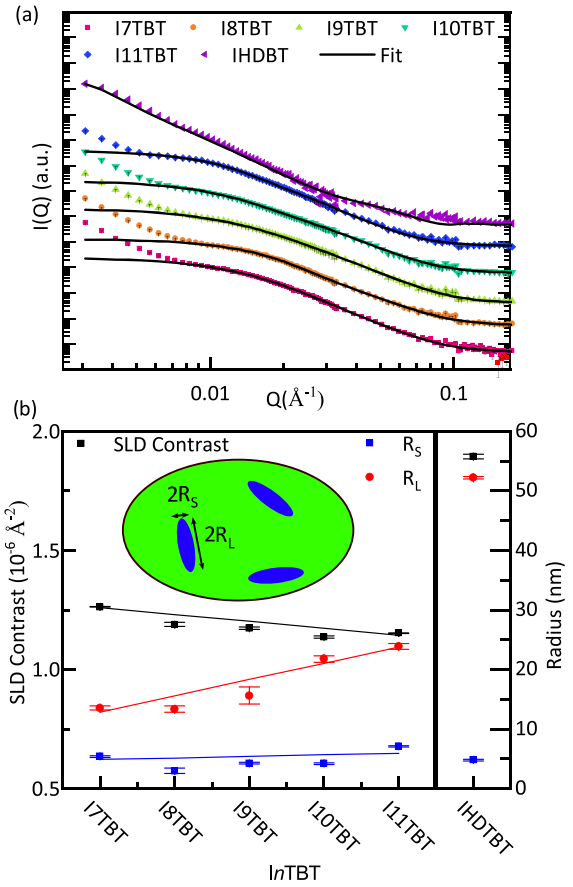

Figure 5. (a) Small-angle neutron scattering data (offset for clarity) of I*n*TBT:PCBM films. I*n*TBTs with linear side chains were fit to an ellipsoidal form factor. IHDTBT was fit with a fuzzy sphere form factor at low Q and a spherical form factor at high Q; the combined fit is plotted. (b) (Left axis) Scattering length density (SLD) contrast (black squares) between the form factor and surrounding matrix. (Right axis) Mean short (R_S) (blue squares) and long (R_L) (red dots) ellipsoidal radii from linear I*n*TBT fits. For IHDTBT, the mean fuzzy sphere radii are plotted as (R_L), and the spherical radii are plotted as (R_S).

Table 3. Volume Fraction of I7TBT and I8TBT in Ellipsoidal and Mixed Domains Obtained from SANS Fits, and Volume Fraction of PCBM in Mixed Domains from Sample Preparation

Merocyanine	$\Phi_{Ellipsoid}^{InTBT}$	Φ_{Mixed}^{InTBT}	Φ_{Mixed}^{PCBM}
I7TBT	0.28	0.21	0.52
I8TBT	0.26	0.24	0.50

increased from 7 to 8 carbons, R_S decreases from 5.3 ± 0.1 to 3.0 ± 0.5 nm and R_L remains consistent at 13.5 ± 0.4 and 13.4 ± 0.6 nm, respectively. So, the needle length is maintained but the diameter narrowed. I8TBT also has more I*n*TBT dispersed in the mixed phase as seen in the decreased SLD contrast from 1.26 to 1.18 × 10^{-6} Å^{-2}. This means that I8TBT has a reduced volume percent of ellipsoidal I*n*TBT domains of 26% compared to that of 28% for I7TBT.

As shown by GIXRD, I*n*TBTs with linear side chains $n \geq 9$ allow PCBM to intercalate into the I*n*TBT crystalline domains, resulting in a further reduction in the SLD contrast. Thus, the model now corresponds to mixed I*n*TBT-rich I*n*TBT:PCBM ellipsoids in a matrix of amorphous PCBM-rich mixed domain. As the linear I*n*TBT side chain is increased from 9 to 10 carbons, R_L increases from 15.6 ± 1.5 to 21.8 ± 0.5 nm and R_S remains consistent at 4.3 ± 0.2 and 4.2 ± 0.2 nm, respectively. So, the mixed crystalline I*n*TBT:PCBM needles become longer while maintaining roughly the same diameter as I8TBT and I7TBT. Interestingly, the I11TBT sample contained the largest ellipsoids in both dimensions with an R_S of 7.1 ± 0.1 nm and an R_L of 23.1 ± 0.5 nm. All of the I*n*TBT films show an increasing scattering intensity through the low Q detector limit. The slope of the intensity increase at low Q follows Porod's law,[39] which suggests the presence of larger structures (>200 nm) in the films that are outside our instrument's measurement range.

SANS data was also collected for IHDTBT:PCBM. The intensity profile was best fit to two models (Figure S26). A spherical form factor was fit to the bend in the spectrum at Q = 0.05 Å^{-1}, and a fuzzy sphere (FS) form factor was fit to the low Q intensity; the combined fit is shown in Figure 5.[37] The spherical radius is 4.8 ± 0.2 nm, plotted as R_S, and the mean FS radius is 52.2 ± 0.2 nm, plotted as R_L. The surface of the FS is smeared with a Gaussian to obtain a gradual drop off in SLD, and the width of the smeared surface interface is 3.7 ± 0.3 nm. Similar to the I*n*TBTs with linear side chains, IHDTBT forms a distribution of domain sizes ranging from 20 to 80 nm (Figure S27). IHDTBT:PCBM films are more phase-segregated resulting in the increased SLD contrast between the FS and the surrounding matrix of 1.89 × 10^{-6} Å^{-2}.

We use AFM to study the mesoscale (25 nm to 5 μm) surface structures on I*n*TBT:PCBM films ($7 \leq n \leq 11$, and n = HD). Figure 6a depicts the height profile and root-mean-square roughness (R_{MS}) of the films. I7TBT:PCBM and IHDTBT:PCBM have the largest R_{MS} of 10.1 ± 0.5 and 7.3 ± 0.5 nm, respectively. These films exhibit depressions in the surface that dig >50% down into the 70 nm films. This is in agreement with SANS and GIXRD; I7TBT and IHDTBT phase-segregate when mixed with PCBM, resulting in increased surface roughness. The I7TBT:PCBM surface shows a connected network of elongated domains with lateral size variations 200 ± 110 nm, while the IHDTBT surface shows round unconnected domains on the order of 240 ± 80 nm. I8TBT:PCBM film surface forms elongated domains (on the size of 210 ± 100 nm) that are less pronounced than the I7TBT:PCBM film and has an R_{MS} of 5.2 ± 0.5 nm. The similar domain size but a reduced fraction of I*n*TBT domains is consistent with the SANS analysis of I7TBT:PCBM and I8TBT:PCBM. Pure I*n*TBT crystals are still present as the side chain is increased to n = 8 but the longer side chain begins to reduce mesoscopic phase segregation. In accordance with GIXRD and SANS, the I9TBT:PCBM, I110TBT:PCBM, and I11TBT:PCBM films form large mixed domains that result in a low R_{MS} of 2.6 ± 0.5, 3.9 ± 0.5, and 3.6 ± 0.5 nm, respectively.

The phase images provide finer detail of the surface composition. Figure 6b shows the corresponding AFM phase images. It is clear that the phase domains for I7TBT:PCBM, I11TBT:PCBM, and IHDTBT:PCBM directly correlate to features observed in the height images. Since I7TBT:PCBM and IHDTBT:PCBM films have the roughest surface topography and the phase shift has a pattern of increasing and decreasing (±10° for I7TBT and ±7.5° for IHDTBT) on the edges of raised surface domains, the observed phase shift is likely an instrument artifact; the tapping AFM tip phase shifts as the tip travels up over a raised surface domain and shifts in

https://dx.doi.org/10.1021/acs.jpcc.0c04988
J. Phys. Chem. C XXXX, XXX, XXX−XXX

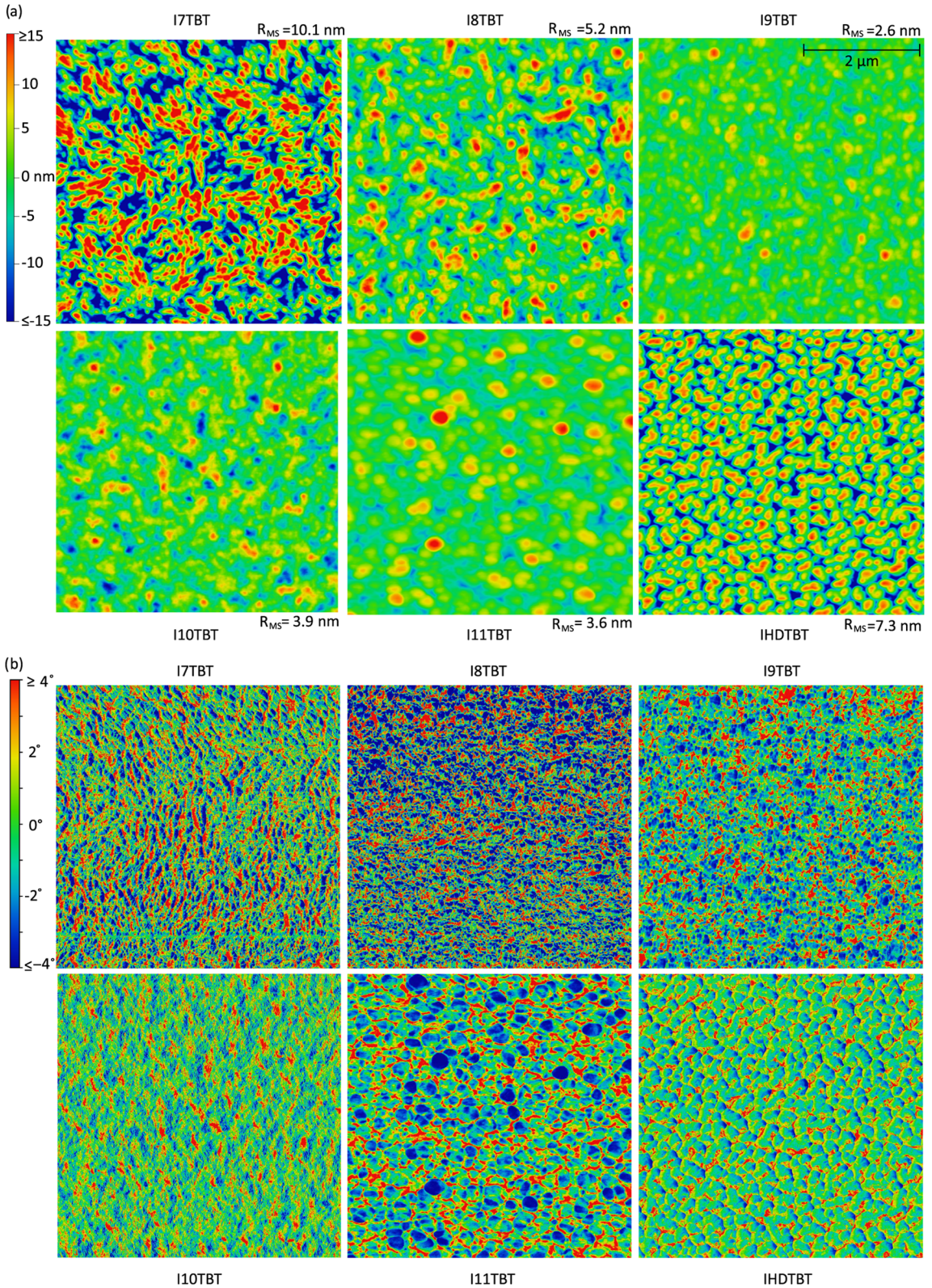

Figure 6. Atomic force microscope (a) height images with mean-square roughness (R_{MS}) and (b) phase images of I*n*TBT:PCBM films.

the opposite direction as the tip travels down into a depression in the film surface. For this reason, we choose to exclude those films from the following phase analysis. This is not observed in the I11TBT:PCBM film due to its lower surface roughness. For I11TBT:PCBM, the raised domains in the height image are compositionally different from the surrounding film. Figure 7 compares the mean grain sizes extracted from the phase images and R_{MS} from height images. The grains are defined by a cutoff phase shift. Red grains have a >4° phase shift, corresponding to I*n*TBT-rich domains, and blue grains have a <−4° phase shift, corresponding to PCBM-rich domains. Figure 7 depicts the mean blue (PCBM-rich) and red (I*n*TBT-

https://dx.doi.org/10.1021/acs.jpcc.0c04988
J. Phys. Chem. C XXXX, XXX, XXX−XXX

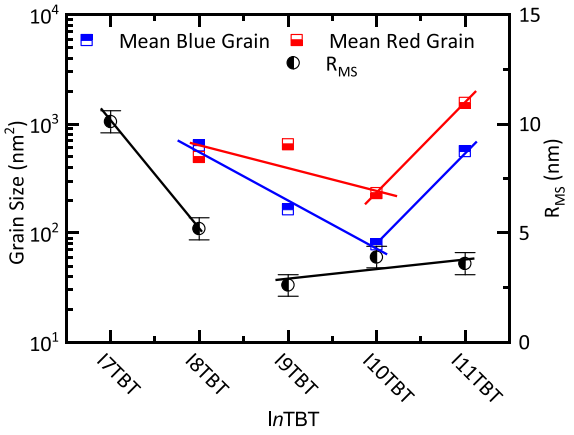

Figure 7. (Left) Mean grain size from AFM phase images of I*n*TBT:PCBM films. Grains are defined by a cutoff phase shift; red (I*n*TBT-rich) grains have a greater than 4° phase shift, and blue (PCBM-rich) grains have a less than −4° phase shift. (Right) Root-mean-square roughness (R_{MS}) from the corresponding AFM height images.

rich) grain sizes; grain size distributions are shown in Figures S28 and S29. Starting with the shortest side-chain film, the I8TBT phase image shows networks of interconnected domains resulting in the relatively large mean PCBM-rich grain size of 630 nm^2 and a mean I*n*TBT-rich grain size of 500 nm^2. As the side chain is increased, I9TBT forms domains with reduced connectivity resulting in mean PCBM-rich and I*n*TBT-rich grain sizes of 160 nm^2 and 650 nm^2, respectively. I10TBT forms a well-mixed film surface resulting in the smoothest phase images with mean PCBM-rich and I*n*TBT-rich grain sizes of 80 nm^2 and 230 nm^2, respectively. As the side chain is increased further, the I11TBT films begin to form large disconnected domains with mean PCBM-rich and I*n*TBT-rich grain sizes of 560 nm^2 and 1540 nm^2, respectively.

DISCUSSION

This series of I*n*TBTs with varying linear side-chain length demonstrates the morphologically controlled balance between exciton dissociation, charge carrier transport, and recombination. A generated exciton can diffuse up to 10 nm before geminate recombination (GR) occurs.[40,41] Charge separation is maximized when the I*n*TBT domain size is minimized to increase the probability of an exciton being generated within 5−10 nm of a I*n*TBT/PCBM interface.[40,41] However, there is a necessary balance between exciton dissociation and free charge carrier transport. Small disconnected I*n*TBT domains reduce hole transport through the film and increase trap sites for free charge carriers, increasing nongeminate recombination (NGR) rates.[42]

Figure 8 illustrates the bulk morphologies reported by GIXRD and SANS for I8TBT:PCBM, I9TBT:PCBM, and I11TBT:PCBM. The PCBM coherence length remains constant at 1.6 nm. I8TBT:PCBM films form pure MC ellipsoids (R_S = 3 nm, R_L = 14 nm) composed of crystalline MC domains with a large MC coherence length (8.7 nm), which are surrounded by a mixed MC:PCBM domain. I9TBT:PCBM films form larger mixed ellipsoids (R_S = 4 nm, R_L = 16 nm) with a shorter MC coherence length (1.1 nm), also surrounded by a mixed MC:PCBM domain. Finally, I11TBT:PCBM films form even larger, more mixed ellipsoids (R_S = 7 nm, R_L = 23 nm), composed of MC crystalline regions with increased coherence length (4.2 nm).

GIXRD shows that I6TBT through I8TBT form pure crystalline phases in I*n*TBT:PCBM films. When the side-chain length is increased to $n \geq 9$, PCBM mixes with I*n*TBT, significantly broadening the observed diffraction peaks. Of the I*n*TBTs with linear side chains, I6TBT:PCBM films have the lowest FF and V_{OC}. GIXRD demonstrates the presence of small unmixed I6TBT domains (L_C = 4.1 nm), which results in high geminate recombination rates. Since our BHJs were fabricated with a 2:3 I*n*TBT:PCBM weight fraction and I6TBT has the lowest molecular weight out of the studied materials, BHJs with I6TBT have the highest molar ratio of I*n*TBT to PCBM. This resulted in a stronger absorbance and the highest J_{SC} of 8.29 mA/cm^2. Likewise, I12TBT:PCBM films have the lowest molar ratio of I*n*TBT to PCBM resulting in the lowest J_{SC} of 6.20 mA/cm^2. GIXRD shows that the 12-carbon linear side chain on I12TBT allows strong mixing between I12TBT and PCBM, which resulted in lower V_{OC} and FF. Since BHJs with I6TBT and I12TBT show reduced PCE due to little and

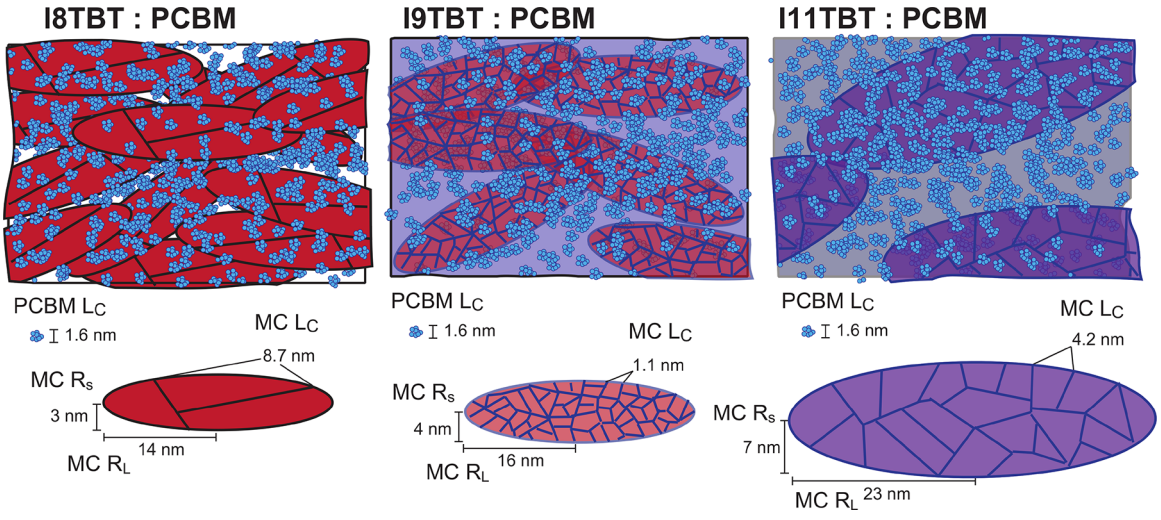

Figure 8. Illustration representing the bulk morphological differences observed between I8TBT:PCBM, I9TBT:PCBM, and I11TBT:PCBM films. L_C is the coherence length from GIXRD, and R_S and R_L are the short and long ellipsoidal radii from SANS, respectively.

https://dx.doi.org/10.1021/acs.jpcc.0c04988
J. Phys. Chem. C XXXX, XXX, XXX−XXX

too much mixing, respectively, we chose to exclude I6TBT and I12TBT from further morphological analysis.

I7TBT and I8TBT BHJs have the same V_{OC} = 0.89 V. They both form pure crystalline domains when mixed with PCBM with an L_C of 7.5 nm and 8.7 nm, respectively. The SANS data shows an R_L of ∼ 5 nm for all films, which should mean that all excitons can reach a donor/acceptor interface, minimizing GR. The topography of the I7TBT:PCBM film shows a larger surface roughness than that of I8TBT:PCBM due to decreased miscibility. The I8TBT:PCBM film has fewer pure I*n*TBT domains and more I*n*TBT in the mixed phase leading to increases in J_{SC} and FF. Finally, the I8TBT:PCBM film has the highest PCE of 4.5%, due to a combination of high J_{SC} and FF.

OPV devices with I9TBT, I10TBT, and I11TBT have the same V_{OC} = 0.90 V. They do not form pure crystalline domains when mixed with PCBM and have a much lower coherence length than I7TBT or I8TBT BHJs for both I*n*TBT and PCBM-rich domains. Curiously, in spite of the increased domain size and the onset of I*n*TBT:PCBM mixing with increased side-chain length, the *JV* characteristics show a remarkably consistent and smooth trend in device characteristics, with V_{OC} peaking for n = 9−11, J_{SC} peaking for n = 8, and FF peaking for n = 11. Thus, I9TBT:PCBM films also produce the highest PCE of 4.5%, even though GIXRD and AFM show that they form an entirely different structural motif compared to I8TBT:PCBM films. SANS demonstrates that I*n*TBTs with $n \geq 9$ form ellipsoidal I*n*TBT domains with reduced SLD contrast due to the presence of PCBM in both the ellipsoid and the surrounding matrix. The J_{SC} decreases with $n > 8$ because the increased side-chain length effectively means a lower absorption coefficient for the 2:3 I*n*TBT:PCBM film. The increase of FF with increased n may be due to a relative volume percent increase of the acceptor.[43]

In spite of the most favorable absorbance, the branched side IHDTBT:PCBM device exhibited the worst OPV performance due to unfavorable morphology across several orders of magnitude. GIXRD shows that the long-branched side chains inhibit intercalation of the PCBM into IHDTBT domains. This is confirmed by the increased SLD contrast from SANS. It should be noted that an increased SLD contrast is also caused by increased ^{1}H density on the longer side chains. SANS demonstrates the presence of small ∼10 nm IHDTBT domains; however, both SANS and AFM show that IHDTBT forms large pure domains on the order of 100−240 nm, significantly increasing the geminate recombination rates, which results in a low J_{SC} of 2.03 mA/cm^2 and a PCE of 0.6%.

It is useful to speculate what the device optimization and morphology assessment performed here indicates regarding the device efficiency limits for I*n*TBT:PCBM OPVs. V_{OC} is quite high at 0.9 V and essentially the same for all linear I*n*TBTs; therefore, it does not need to be optimized. Our analysis fixed the OPV layer thickness at 70 nm and wt ratio of I*n*TBT:PCBM at 2:3 because these parameters came from a prior optimization of MC:PCBM solubility.[27] The trend in FF indicates that the hole and electron currents are well balanced with little bimolecular recombination in films up to a 70 nm device thickness. With such high FF and no optimization of the mixing ratio, it is likely that layer thicknesses of up to ∼ 200 nm would still have FF above 0.6. Given the absorbance of up to ∼ 725 nm (which is ∼1.7 eV), one could expect a J_{SC} of up to 15 mA/cm^2 under AM1.5 illumination and an optimized PCE of 6.5−8%.[44]

Another intriguing series of future experiments should focus on mixing multiple different I*n*TBTs with fullerenes. Since the I*n*TBTs form mixed structures for $n \geq 9$ and $n \leq 8$ form pure domains, one could exert far more control over the morphology using a combination of I*n*TBTs with mixed side-chain lengths to obtain even greater improvements to the FF.

Although PCEs reported in this manuscript could be considered relatively low compared to recent record small-molecule devices, we point out that D−A MC dyes are extremely inexpensive. Previous small-molecule OPV studies claim that D−A−D-like structures are needed to prevent dipole alignment between neighboring molecules to obtain high PCEs. However, we demonstrate that decent PCEs can be obtained through morphological optimization of D−A systems and that the miscibility with a PCBM acceptor can be tuned through a range of domain sizes and mixing ratios.

CONCLUSIONS

This manuscript demonstrates a novel series of MC dyes with varying hydrocarbon side-chain length. BHJ OPV devices were fabricated with a 2:3 wt ratio of I*n*TBT:PCBM and characterized as a function of side-chain length. A maximum PCE of 4.5 ± 0.1% was extracted from I8TBT:PCBM and I9TBT:PCBM devices. As expected, tuning the side-chain length allows careful adjustment of the miscibility between the donor and acceptor, thereby enabling optimization of film morphology and OPV performance characteristics. Hierarchical structure formation was studied using GIXRD (Å), SANS (3−200 nm), and AFM (25−5 μm). When mixed with PCBM, I*n*TBTs with ≤ 8 side-chain carbons form pure crystalline domains, while I*n*TBTs with ≥9 side-chain carbons form mixed domains with PCBM. SANS demonstrates that increasing side-chain length increases the I*n*TBT-rich domain size while at the same time allowing for mixed domains for $n \geq 9$. The branched side-chain IHDTBT:PCBM film was also studied and was found to exhibit the worst-performance OPV device; the large side chain inhibited mixing between IHDTBT and PCBM resulting in large segregated phases. Further optimization of the mixing ratios and layer thickness could nearly double the OPV performance. Ternary mixtures of I*n*TBTs with different side-chain lengths could enable even more control over the BHJ morphology.

ASSOCIATED CONTENT

Supporting Information

The Supporting Information is available free of charge at https://pubs.acs.org/doi/10.1021/acs.jpcc.0c04988.

Synthesis, ultraviolet−visible spectroscopy, crystal stacking, grazing incidence X-ray diffraction analysis, small-angle neutron scattering analysis, and atomic force microscopy analysis (PDF)

AUTHOR INFORMATION

Corresponding Authors

Adam J. Moulé − *Department of Chemical Engineering, University of California, Davis, California 95616, United States;* orcid.org/0000-0003-1354-3517; Email: amoule@ucdavis.edu

Klaus Meerholz − *Department für Chemie, Universität zu Köln, 50939 Köln, Germany*; Email: klaus.meerholz@uni-koeln.de

https://dx.doi.org/10.1021/acs.jpcc.0c04988
J. Phys. Chem. C XXXX, XXX, XXX−XXX

Authors

Tucker L. Murrey − *Department of Material Science and Engineering, University of California, Davis, California 95616, United States;* orcid.org/0000-0002-5947-2892

Dirk Hertel − *Department für Chemie, Universität zu Köln, 50939 Köln, Germany*

Julian Nowak − *Department für Chemie, Universität zu Köln, 50939 Köln, Germany*

Ruth Bruker − *Department für Chemie, Universität zu Köln, 50939 Köln, Germany*

Thorsten Limböck − *Department für Chemie, Universität zu Köln, 50939 Köln, Germany*

Jörg Neudörfl − *Department für Chemie, Universität zu Köln, 50939 Köln, Germany*

Stephanie Rüth − *Department für Chemie, Universität zu Köln, 50939 Köln, Germany*

Jürgen Schelter − *Department für Chemie, Universität zu Köln, 50939 Köln, Germany*

Selina Olthof − *Department für Chemie, Universität zu Köln, 50939 Köln, Germany;* orcid.org/0000-0002-8871-1549

Aurel Radulescu − *Jülich Centre for Neutron Science, Heinz Maier-Leibnitz Zentrum, Forschungszentrum Jülich GmbH, 85748 Garching, Germany*

Complete contact information is available at: https://pubs.acs.org/10.1021/acs.jpcc.0c04988

Notes

The authors declare no competing financial interest.

■ ACKNOWLEDGMENTS

This project was supported by the U.S. Department of Energy, Office of Basic Energy Sciences, Division of Materials Sciences and Engineering, under Award No. DE-SC0010419, and the German Federal Office of Science and Technology (BMBF, MEDOS FKZ: 03EK3505I). The authors thank the Alexander von Humboldt Foundation and the Universität zu Köln alumni fellowship fund for sabbatical funding for A.J.M. The authors also thank the Jülich Centre for Neutron Science at Heinz Maier-Leibnitz Zentrum in Garching, Germany, for small-angle neutron scattering measurement time. This work benefited from the use of the SasView application, originally developed under NSF award DMR-0520547. SasView contains the code developed with funding from the European Union's Horizon 2020 research and innovation programme under the SINE2020 project, grant agreement no. 654000.

■ REFERENCES

(1) Roncali, J.; Leriche, P.; Blanchard, P. Molecular Materials for Organic Photovoltaics: Small is Beautiful. *Adv. Mater.* **2014**, *26*, 3821−3838.

(2) Augulis, R.; Devizis, A.; Peckus, D.; Gulbinas, V.; Hertel, D.; Meerholz, K. High Electron Mobility and Its Role in Charge Carrier Generation in Merocyanine/Fullerene Blends. *J. Phys. Chem. C* **2015**, *119*, 5761−5770.

(3) Arjona-Esteban, A.; Krumrain, J.; Liess, A.; Stolte, M.; Huang, L.; Schmidt, D.; Stepanenko, V.; Gsanger, M.; Hertel, D.; Meerholz, K.; et al. Influence of Solid-State Packing of Dipolar Merocyanine Dyes on Transistor and Solar Cell Performances. *J. Am. Chem. Soc.* **2015**, *137*, 13524−13534.

(4) Kronenberg, N. M.; Bürckstümmer, H.; Deppisch, M.; Würthner, F.; Meerholz, K. Optimized Solution-Processed Merocyanine:PCBM Organic Bulk Heterojunction Solar Cell. *J. Photonics Energy* **2011**, *1*, No. 011101.

(5) Ghosh, A. K.; Feng, T. Merocyanine Organic Solar Cells. *J. Appl. Phys.* **1978**, *49*, 5982−5989.

(6) Würthner, F.; Meerholz, K. Systems Chemistry Approach in Organic Photovoltaics. *Chem. − Eur. J.* **2010**, *16*, 9366−9373.

(7) Mishra, A.; Bauerle, P. Small Molecule Organic Semiconductors on the Move: Promises for Future Solar Energy Technology. *Angew. Chem., Int. Ed.* **2012**, *51*, 2020−2067.

(8) Lin, Y.; Li, Y.; Zhan, X. Small Molecule Semiconductors for High-Efficiency Organic Photovoltaics. *Chem. Soc. Rev.* **2012**, *41*, 4245−4272.

(9) Li, Y.; Guo, Q.; Li, Z.; Pei, J.; Tian, W. Solution Processable D-A Small Molecules for Bulk-Heterojunction Solar Cells. *Energy Environ. Sci.* **2010**, *3*, 1427−1436.

(10) Liess, A.; Arjona-Esteban, A.; Kudzus, A.; Albert, J.; Krause, A.-M.; Lv, A.; Stolte, M.; Meerholz, K.; Wrthner, F. Ultranarrow Bandwidth Organic Photodiodes by Exchange Narrowing in Merocyanine H- and J-Aggregate Excitonic Systems. *Adv. Funct. Mater.* **2019**, *29*, No. 1805058.

(11) Kronenberg, N. M.; Deppisch, M.; Würthner, F.; Lademann, H. W. A.; Deing, K.; Meerholz, K. Bulk Heterojunction Organic Solar Cells Based on Merocyanine Colorants. *Chem. Commun.* **2008**, 6489−6491.

(12) Steinmann, V.; Kronenberg, N. M.; Lenze, M. R.; Graf, S. M.; Hertel, D.; Bürckstümmer, H.; Würthner, F.; Meerholz, K. A simple Merocyanine Tandem Solar Cell with Extraordinarily High Open-Circuit Voltage. *Appl. Phys. Lett.* **2011**, *99*, No. 193306.

(13) Steinmann, V.; Kronenberg, N. M.; Lenze, M. R.; Graf, S. M.; Hertel, D.; Meerholz, K.; Bürckstümmer, H.; Tulyakova, E. V.; Würthner, F. Simple, Highly Efficient Vacuum-Processed Bulk Heterojunction Solar Cells Based on Merocyanine Dyes. *Adv. Energy Mater.* **2011**, *1*, 888−893.

(14) Bürckstümmer, H.; Tulyakova, E. V.; Deppisch, M.; Lenze, M. R.; Kronenberg, N. M.; Gsanger, M.; Stolte, M.; Meerholz, K.; Würthner, F. Efficient Solution-Processed Bulk Heterojunction Solar Cells by Antiparallel Supramolecular Arrangement of Dipolar Donor-Acceptor Dyes. *Angew. Chem., Int. Ed.* **2011**, *50*, 11628−11632.

(15) Gräßler, N.; Wolf, S.; Holzmüller, F.; Zeika, O.; Vandewal, K.; Leo, K. Heteroquinoid Merocyanine Dyes with High Thermal Stability as Absorber Materials in Vacuum-Processed Organic Solar Cells. *Eur. J. Org. Chem.* **2019**, *2019*, 845−851.

(16) Wang, Z.; Zhu, L.; Shuai, Z.; Wei, Z. A-π-D-π-A Electron-Donating Small Molecules for Solution-Processed Organic Solar Cells: A Review. *Macromol. Rapid Commun.* **2017**, *38*, No. 1700470.

(17) Zhou, R.; Jiang, Z.; Yang, C.; Yu, J.; Feng, J.; Adil, M. A.; Deng, D.; Zou, W.; Zhang, J.; Lu, K.; et al. All-Small-Molecule Organic Solar Cells with Over 14. *Nat. Commun.* **2019**, *10*, No. 5393.

(18) Menke, S. M.; Holmes, R. J. Exciton Diffusion in Organic Photovoltaic Cells. *Energy Environ. Sci.* **2014**, *7*, 499−512.

(19) Hestand, N. J.; Spano, F. C. Expanded Theory of H- and J-Molecular Aggregates: The Effects of Vibronic Coupling and Intermolecular Charge Transfer. *Chem. Rev.* **2018**, *118*, 7069−7163.

(20) Chang, M.; Meng, L.; Wang, Y.; Ke, X.; Yi, Y.-Q.-Q.; Zheng, N.; Zheng, W.; Xie, Z.; Zhang, M.; Yi, Y.; et al. Achieving an Efficient and Stable Morphology in Organic Solar Cells Via Fine-Tuning the Side Chains of Small-Molecule Acceptors. *Chem. Mater.* **2020**, *32*, 2593−2604.

(21) Qiu, B.; Chen, S.; Xue, L.; Sun, C.; Li, X.; Zhang, Z.-G.; Yang, C.; Li, Y. Effects of Alkoxy and Fluorine Atom Substitution of Donor Molecules on the Morphology and Photovoltaic Performance of All Small Molecule Organic Solar Cells. *Front. Chem.* **2018**, *6*, 413.

(22) Jurow, M. J.; Hageman, B. A.; DiMasi, E.; Nam, C.-Y.; Pabon, C.; Black, C. T.; Drain, C. M. Controlling Morphology and Molecular Packing of Alkane Substituted Phthalocyanine Blend Bulk Heterojunction Solar Cells. *J. Mater. Chem. A* **2013**, *1*, 1557−1565.

(23) Krause, L.; Herbst-Irmer, R.; Sheldrick, G. M.; Stalke, D. Comparison of Silver and Molybdenum Microfocus X-ray Sources for Single-Crystal Structure Determination. *J. Appl. Crystallogr.* **2015**, *48*, 3−10.

(24) Sheldrick, G. M. SHELXT − Integrated space-group and crystal-structure determination. *Acta Crystallogr., Sect. A: Found. Crystallogr.* **2015**, *71*, 3−8.
(25) Elschner, C.; Levin, A. A.; Wilde, L.; Grenzer, J.; Schroer, C.; Leo, K.; Riede, M. Determining the C60 Molecular Arrangement in Thin Films by Means of X-ray Diffraction. *J. Appl. Crystallogr.* **2011**, *44*, 983−990.
(26) Kronenberg, N. M.; Steinmann, V.; Bürckstümmer, H.; Hwang, J.; Hertel, D.; Würthner, F.; Meerholz, K. Direct Comparison of Highly Efficient Solution- and Vacuum-Processed Organic Solar Cells Based on Merocyanine Dyes. *Adv. Mater.* **2010**, *22*, 4193−4197.
(27) Lenze, M. R.; Kronenberg, N. M.; Würthner, F.; Meerholz, K. In-situ Modification of PEDOT:PSS Work Function using Alkyl Alcohols as Secondary Processing Solvents and their Impact on Merocyanine Based Bulk Heterojunction Solar Cells. *Org. Electron.* **2015**, *21*, 171−176.
(28) Qi, B.; Wang, J. Fill Factor in Organic Solar Cells. *Phys. Chem. Chem. Phys.* **2013**, *15*, 8972−8982.
(29) Jao, M.-H.; Liao, H.-C.; Su, W.-F. Achieving a High Fill Factor for Organic Solar Cells. *J. Mater. Chem. A* **2016**, *4*, 5784−5801.
(30) Sánchez-Bajo, F.; Cumbrera, F. L. The Use of the Pseudo-Voigt Function in the Variance Method of X-ray Line-Broadening Analysis. *J. Appl. Crystallogr.* **1997**, *30*, 427−430.
(31) Olivero, J.; Longbothum, R. Empirical Fits to the Voigt Line Width: A Brief Review. *J. Quant. Spectrosc. Radiat. Transfer* **1977**, *17*, 233−236.
(32) Bragg, W. H.; Bragg, W. L. The Reflection of X-rays by Crystals. *Proc. R. Soc. London, Ser. A* **1913**, *88*, 428−438.
(33) Patterson, A. L. The Scherrer Formula for X-Ray Particle Size Determination. *Phys. Rev.* **1939**, *56*, 978−982.
(34) Rivnay, J.; Noriega, R.; Kline, R. J.; Salleo, A.; Toney, M. F. Quantitative Analysis of Lattice Disorder and Crystallite Size in Organic Semiconductor Thin Films. *Phys. Rev. B* **2011**, *84*, No. 045203.
(35) Mens, R.; Chambon, S.; Bertho, S.; Reggers, G.; Ruttens, B.; D'Haen, J.; Manca, J.; Carleer, R.; Vanderzande, D.; Adriaensens, P. Description of the Nanostructured Morphology of [6,6]-Phenyl-C61-Butyric Acid Methyl Ester (PCBM) by XRD, DSC and Solid-State NMR. *Magn. Reson. Chem.* **2011**, *49*, 242−247.
(36) Toyoko, I.; Toshiji, K.; Michihiro, F.; Naoya, T. *Neutrons in Soft Matter*; Wiley, 2011.
(37) Feigin, L. A.; Svergun, D. I. *Structure Analysis by Small-Angle X-Ray and Neutron Scattering*; Taylor, G. W., Ed.; Springer, 1987.
(38) Clulow, A. J.; Armin, A.; Lee, K. H.; Pandey, A. K.; Tao, C.; Velusamy, M.; James, M.; Nelson, A.; Burn, P. L.; Gentle, I. R.; et al. Determination of Fullerene Scattering Length Density: A Critical Parameter for Understanding the Fullerene Distribution in Bulk Heterojunction Organic Photovoltaic Devices. *Langmuir* **2014**, *30*, 1410−1415.
(39) Sinha, S. K.; Sirota, E. B.; Garoff, S.; Stanley, H. B. X-ray and Neutron Scattering from Rough Surfaces. *Phys. Rev. B* **1988**, *38*, 2297−2311.
(40) Dou, L.; You, J.; Hong, Z.; Xu, Z.; Li, G.; Street, R. A.; Yang, Y. 25th Anniversary Article: A Decade of Organic/Polymeric Photovoltaic Research. *Adv. Mater.* **2013**, *25*, 6642−6671.
(41) Wojcik, M.; Nowak, A.; Seki, K. Geminate Electron-Hole Recombination in Organic Photovoltaic Cells. A Semi-Empirical Theory. *J. Chem. Phys.* **2017**, *146*, No. 054101.
(42) Göhler, C.; Wagenpfahl, A.; Deibel, C. Nongeminate Recombination in Organic Solar Cells. *Adv. Electron. Mater.* **2018**, *4*, No. 1700505.
(43) Moulé, A. J.; Bonekamp, J. B.; Meerholz, K. The Effect of Active Layer Thickness and Composition on the Performance of Bulk-Heterojunction Solar Cells. *J. Appl. Phys.* **2006**, *100*, No. 094503.
(44) Scharber, M.; Mhlbacher, D.; Koppe, M.; Denk, P.; Waldauf, C.; Heeger, A.; Brabec, C. Design Rules for Donors in Bulk-Heterojunction Solar Cells Towards 10% Energy-Conversion Efficiency. *Adv. Mater.* **2006**, *18*, 789−794.

https://dx.doi.org/10.1021/acs.jpcc.0c04988
J. Phys. Chem. C XXXX, XXX, XXX−XXX